Experimental Section

Synthesis of In$_1$/a-MoO$_3$

All the chemicals are of analytical grade and used as received. In a typical procedure, 10 mg InCl$_3$, 50 mg of MoO$_3$ and 100 mg of C$_2$H$_2$O$_4$·2H$_2$O were dispersed into 30 mL distilled water under stirring at 90°C for 2 h. The mixture was then subjected to supercritical CO$_2$ treatment at 180 °C under the pressure of 10 MPa for 6 h[1]. After treatment, the resulting products were collected by centrifuging, washing with deionized water/ethanol several times, and drying at 60 °C overnight, obtaining In$_1$/a-MoO$_3$. Bare a-MoO$_3$ was by the same procedure without addition of InCl$_3$.

Electrochemical experiments

Electrochemical measurements were performed on a CHI-660E electrochemical workstation using a conventional three-electrode cell. The catalyst coated on carbon cloth (CC, 0.5 mg cm^{-2}) was used as the working electrode, Ag/AgCl (saturated KCl) electrode was used as the reference electrode, and graphite rod was used as the counter electrode. All potentials were referenced to reversible hydrogen electrode (RHE) by following equation: E_{RHE} (V)=$E_{Ag/AgCl}$+0.198+0.059×pH. Electrochemical NORR tests were performed in 0.5 M Na$_2$SO$_4$ solution using an gas-tight H-type cell separated by a Nafion 211 membrane. The Nafion membrane was pretreated by boiling it in 5% H$_2$O$_2$ solution for 1 h, 0.5 M H$_2$SO$_4$ for 1 h and deionized water for 1 h in turn. Before the NORR test, all feeding gases were purified through two glass bubblers containing 4 M KOH solution and the cathodic compartment was purged with Ar for at least 30 min to remove residual oxygen[2]. During the potentiostatic testing, NO flow (99.9%, 20 mL min^{-1}) was continuously fed to the cathodic compartment. After electrolysis for 1 h at various potentials, liquid and gas products were detected by colorimetry and gas chromatography (GC, Shimadzu GC2010), respectively[3].

Calculations of NH$_3$ yield rate and NH$_3$-Faradaic efficiency

$$\text{NH}_3 \text{ yield rate } (\mu g \text{ h}^{-1} \text{ mg}_{cat.}^{-1}) = \frac{c_{\text{NH}_3} \times V}{t \times A} \tag{1}$$

$$\text{NH}_3\text{-Faradaic efficiency (\%)} = \frac{5 \times F \times c_{\text{NH}_3} \times V}{17 \times Q} \times 100\% \tag{2}$$

where c_{NH3} (μg mL^{-1}) is the measured NH$_3$ concentration, V (mL) is the volume of the electrolyte, t (h) is the reduction time, A (cm^{-2}) is the surface area of CC (1×1 cm^2) , F (96500 C mol^{-1}) is the Faraday constant, Q (C) is the quantity of applied electricity.

Characterizations

Spherical aberration-corrected scanning transmission electron microscopy (AC-STEM) was performed on a Titan Themes Cubed G2 300 microscope. Transmission electron microscopy (TEM), high-resolution transmission electron microscopy (HRTEM), selected area electron diffraction (SAED) and scanning transmission electron microscopy (STEM) were performed on a Tecnai G^2 F20 microscope. X-ray diffraction (XRD) pattern was collected on a Rigaku D/max 2400 diffractometer. On-line differential electrochemical mass spectrometry (DEMS, QAS 100) was performed on a by QAS 100 spectrometer.　The various products during the electrolysis reactions were monitored at different values of m/z ionic signals.

Calculation details

DFT calculations within Cambridge sequential total energy package (CASTEP) code have been performed. The Perdew-Burke-Ernzerhof (PBE) generalized gradient approximation (GGA) functional was used for the exchange-correlation potential. DFT-D method was employed to calculate the van der Waals (vdW) interaction. To ensure the convergence for the total energy, all the calculations were performed using a plane-wave cutoff energy of 400 eV, and a Monkhorst-Pack grid (3 × 3 × 1) was used for k-point sampling. Besides, the convergence thresholds of energy and forces were set to be 1.0×10^{-5} eV and 0.02 eV Å^{-1}, respectively. MoO$_3$ (010) was modeled by a 4 × 4 supercell, and a vacuum region of 15 Å was used to separate adjacent slabs. The amorphous MoO$_3$ was built by relaxing the crystalline MoO$_3$ at 500 K, and the ordered atomic arrangement could be damaged.

The free energies (ΔG, 298 K) for each reaction were given after correction:

$$\Delta G = \Delta E + \Delta ZPE - T\Delta S \tag{3}$$

where ΔE is the adsorption energy, ΔZPE is the zero-point energy difference and $T\Delta S$

is the entropy difference between the gas phase and adsorbed state.

MD simulations were carried out using a force field type of universal. The electrolyte system was modeled by a cubic cell with placing catalyst at the center of the cell and randomly filling 1000 H_2O, 50 NO, and 50 H. After geometry optimization, the MD simulations were performed in an NVT ensemble (298 K) with the total simulation time of 1 ns at a time step of 1 fs.

The radial distribution function (RDF) is calculated as

$$g(r) = \frac{dN}{4\pi\rho r^2 dr} \tag{4}$$

where dN is the amount of NO in the shell between the central particle r and $r+dr$, ρ is the number density of NO and H.
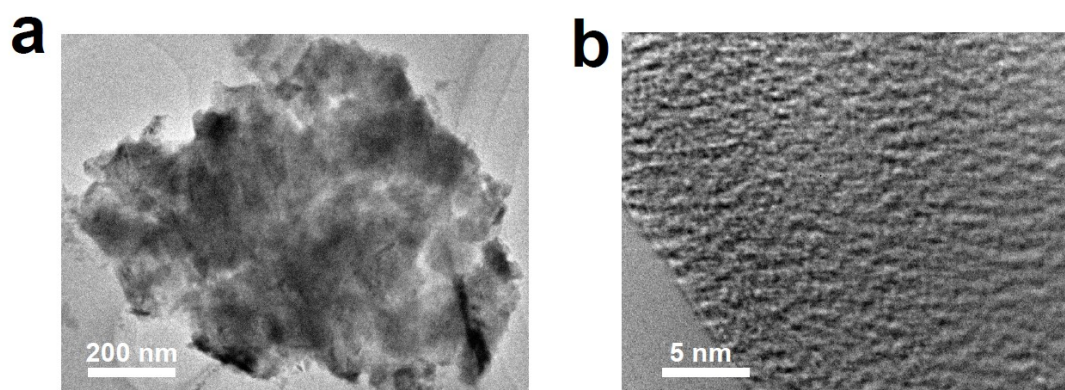
Fig. S1. (a) TEM and (b) HRTEM images of bare a-MoO$_3$.
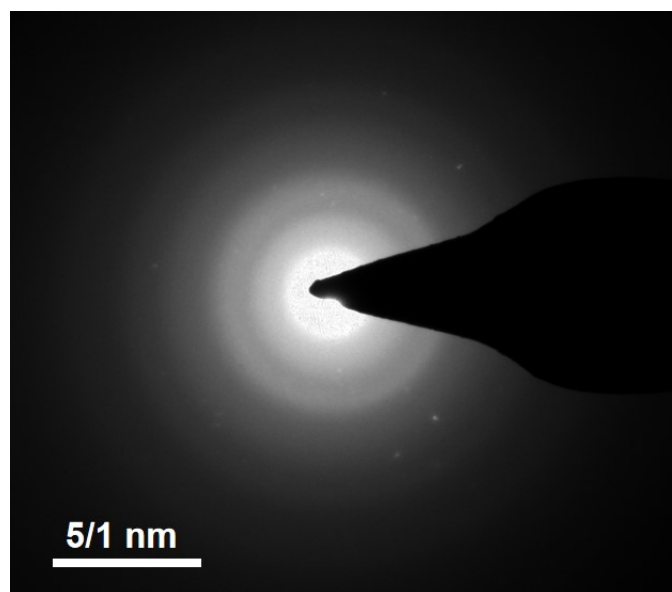
Fig. S2. SAED pattern of In$_1$/a-MoO$_3$.

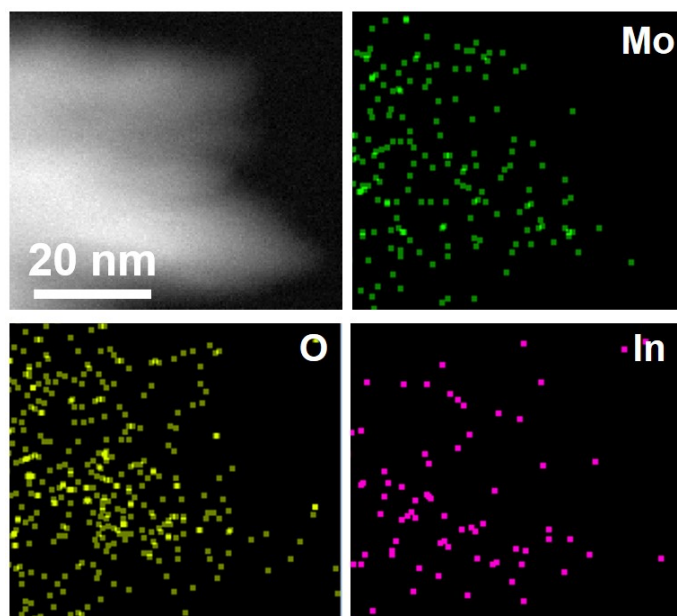Fig. S3. STEM element mapping images of In_1/a-MoO_3.

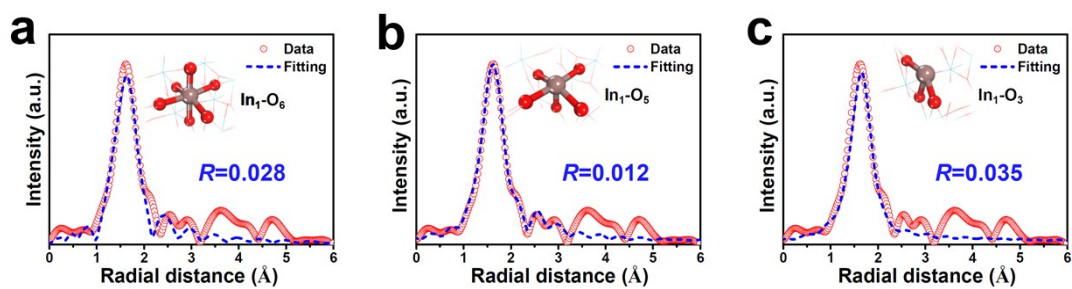Fig. S4. EXAFS fitting curves of $In_1/a-MoO_3$ with three possible models
(a) In_1-O_6, (b) In_1-O_5, (c) In_1-O_3.

We use three most possible models (In_1-O_6, In_1-O_5 and In_1-O_3) to conduct the EXAFS fitting of $In_1/a-MoO_3$ (note that the models of In_1-O_4, In_1-O_2 and In_1-O_1 are thermodynamic unstable). It is seen in Fig. S4 that the fitting goodness (R) of In_1-O_5 is the smallest, which means that single-atomic In is mostly likely to be coordinated with five O atoms to form In_1-O_5 motif.
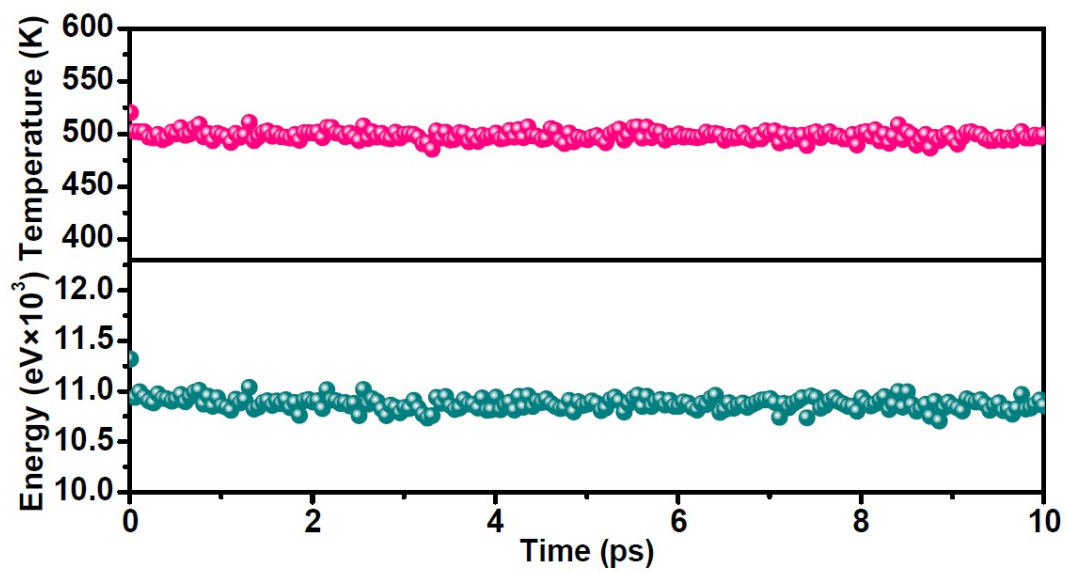
Fig. S5. Variations of energy and temperature during the ab initio molecular dynamics (AIMD) simulations for assessing the thermodynamic stability of In_1/a-MoO_3.
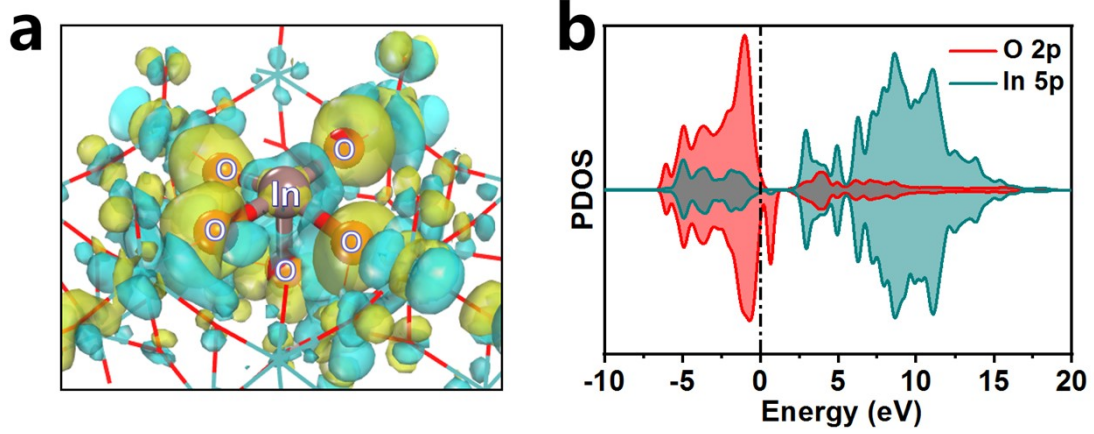
Fig. S6. (a) Charge density difference (yellow: charge accumulation, cyan: charge depletion) and (b) PDOS profile of In_1-O_5 motif in In_1/a-MoO_3.

It is seen that the charge density difference (Fig. S5a) presents a strong In/O electronic interaction in In_1-O_5 motif, and this can be further confirmed by the remarkable In/O orbital hybridization in the PDOS analysis (Fig. S5b).
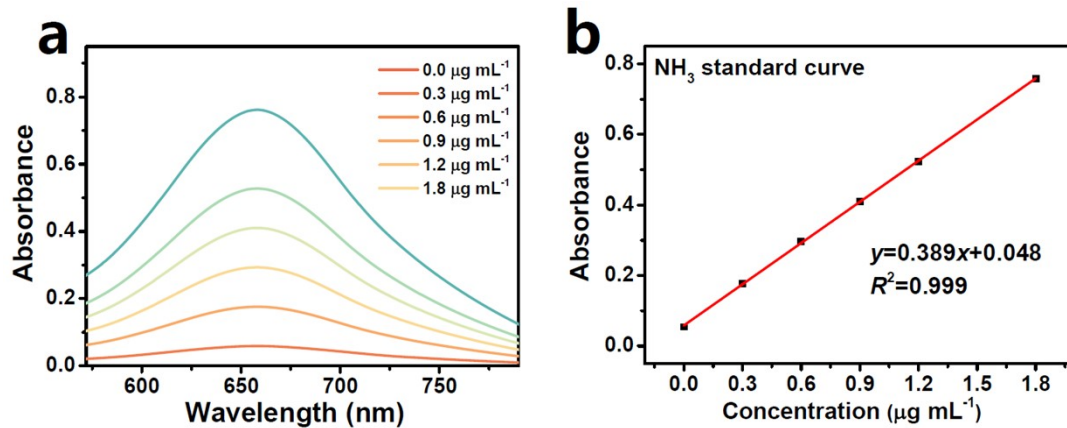
Fig. S7. (a) UV-vis absorption spectra of NH_4^+ assays after incubated for 2 h at ambient conditions. (b) Calibration curve used for the calculation of NH_3 concentrations.
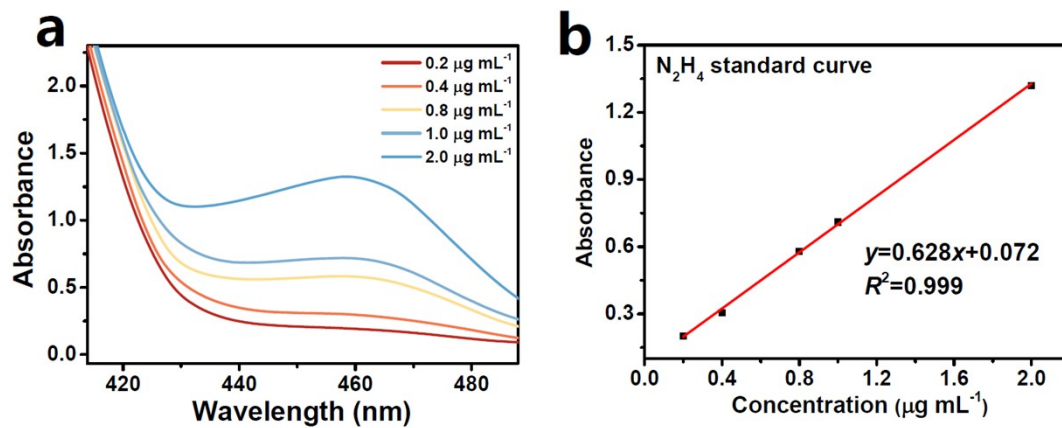
Fig. S8. (a) UV-vis absorption spectra of N_2H_4 assays after incubated for 20 min at ambient conditions. (b) Calibration curve used for calculation of N_2H_4 concentrations.
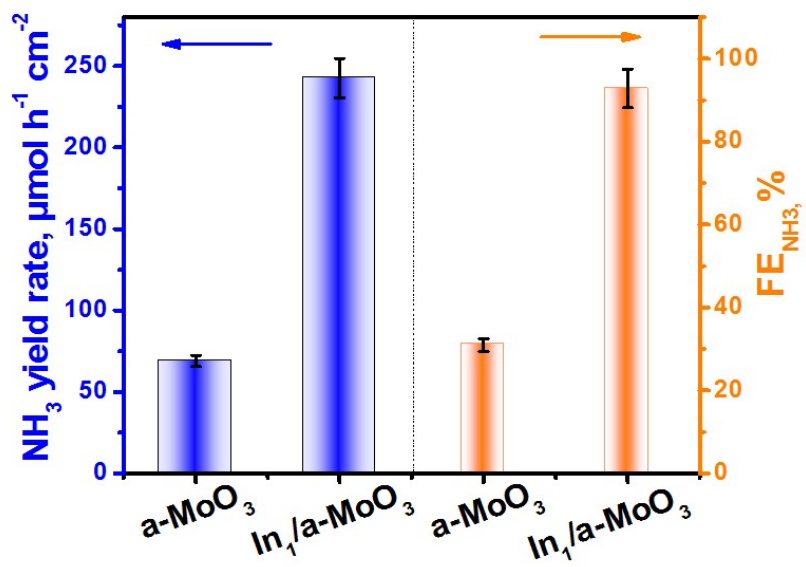
Fig. S9. Comparison of the NORR performance between bare a-MoO$_3$ and In$_1$/a-MoO$_3$ at -0.6 V.
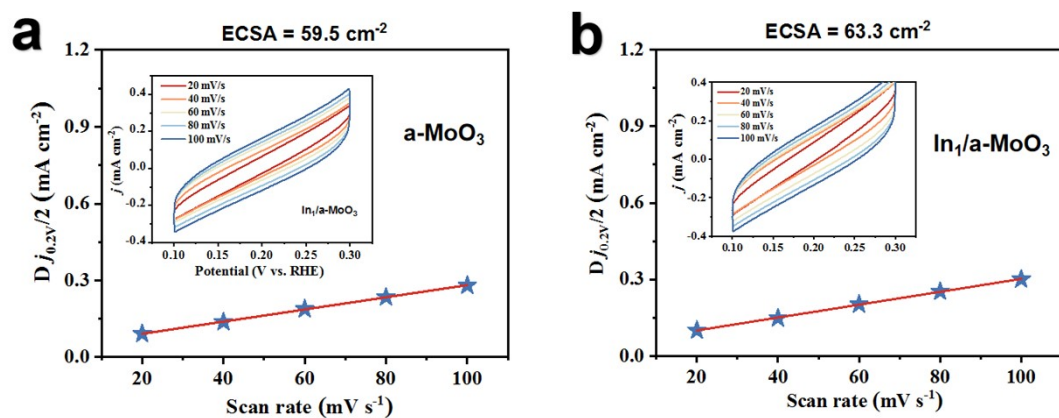
Fig. S10. CV measurements at different scanning rates and calculated ECSA values for (a) a-MoO$_3$, (b) In$_1$/a-MoO$_3$.

It is seen that the electrochemically active surface area (ECSA) values are comparable between a-MoO$_3$ (59.5 cm^{-2}) and In$_1$/a-MoO$_3$ (63.3 cm^{-2}), which means that the introduced In single atoms have little impact on the ECSA. Thus, In$_1$/a-MoO$_3$ has an intrinsically higher NORR activity than bare a-MoO$_3$.
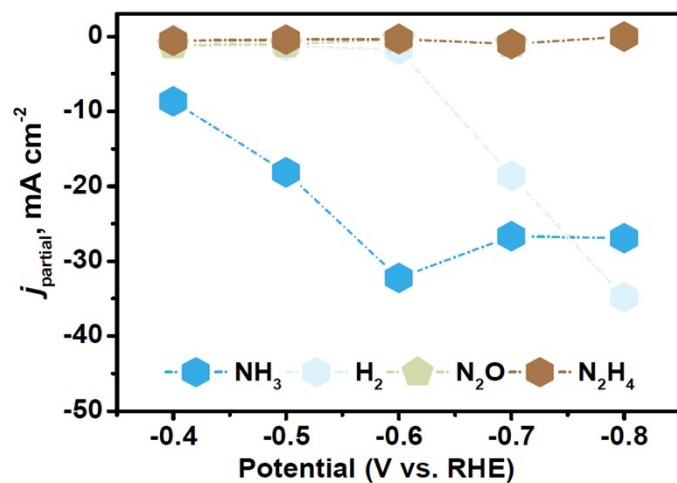
Fig. S11. Partial current densities of various products over In$_1$/a-MoO$_3$ after 1 h of NORR electrolysis at different potentials.
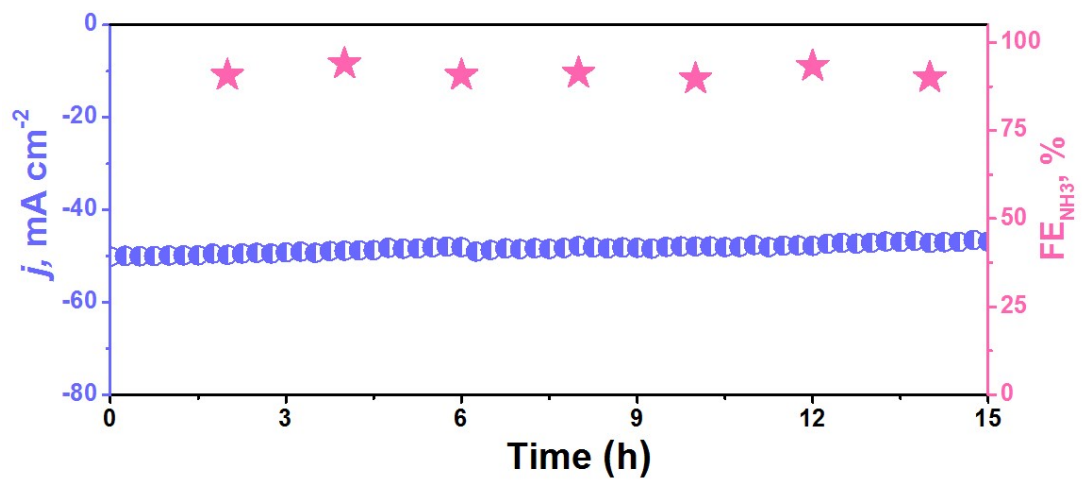
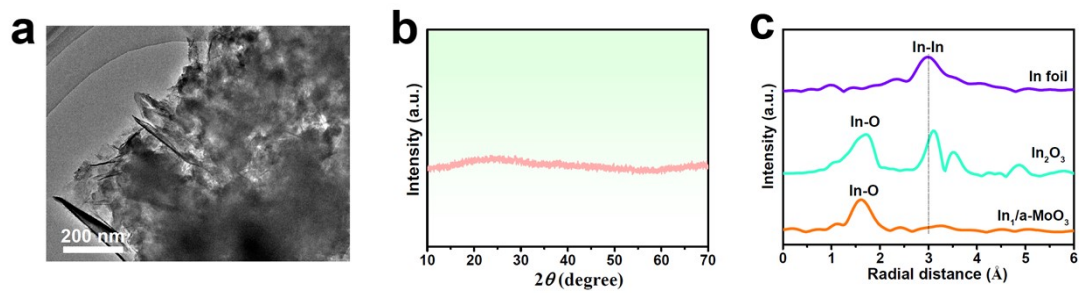Fig. S12. Chronopotentiometric test of In_1/a-MoO_3 for 15 h at -0.6 V.

Fig. S13. (a) TEM image, (b) XRD pattern and (c) In K-edge EXAFS spectra of In$_1$/a-MoO$_3$ after stability test.

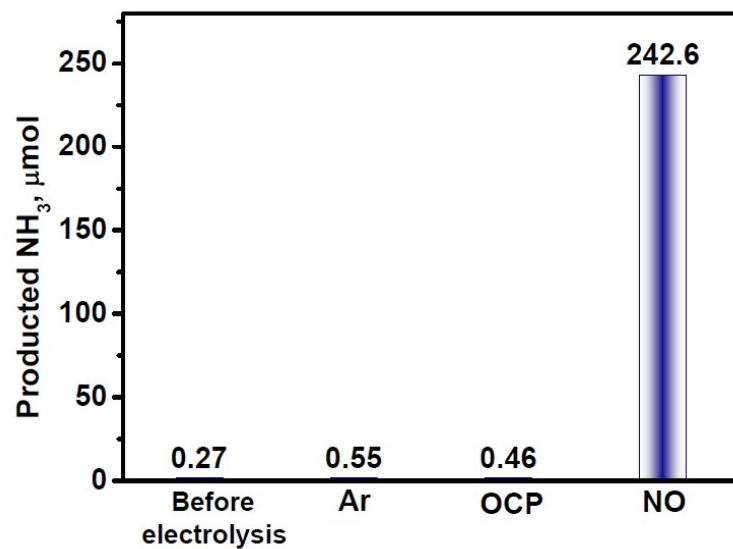Fig. S14. Amounts of produced NH_3 on In_1/a-MoO_3 under different conditions: (1) before electrolysis; (2) electrolysis on In_1/a-MoO_3 in Ar-saturated electrolyte at -0.6 V; (3) electrolysis on In_1/a-MoO_3 in NO-saturated electrolyte at open-circuit potential; (4) electrolysis on In_1/a-MoO_3 in NO-saturated electrolyte at -0.6 V.
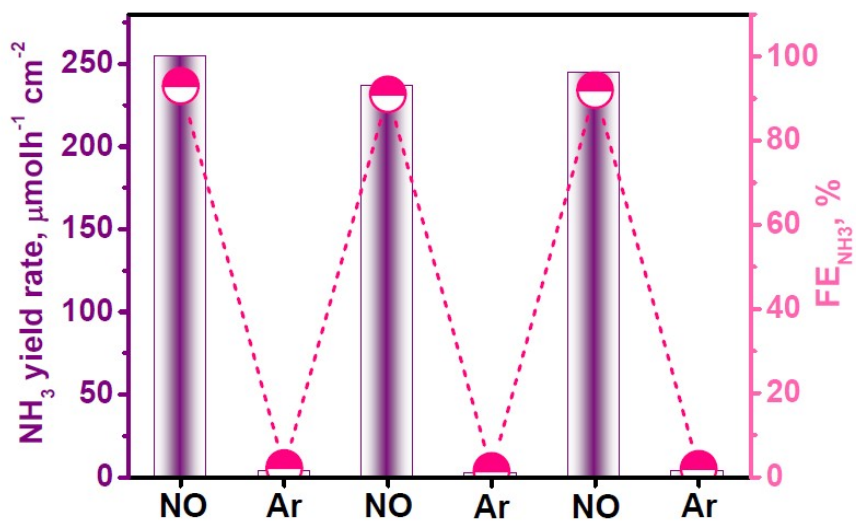
Fig. S15. NO-Ar switching test on In_1/a-MoO_3 at -0.6 V.
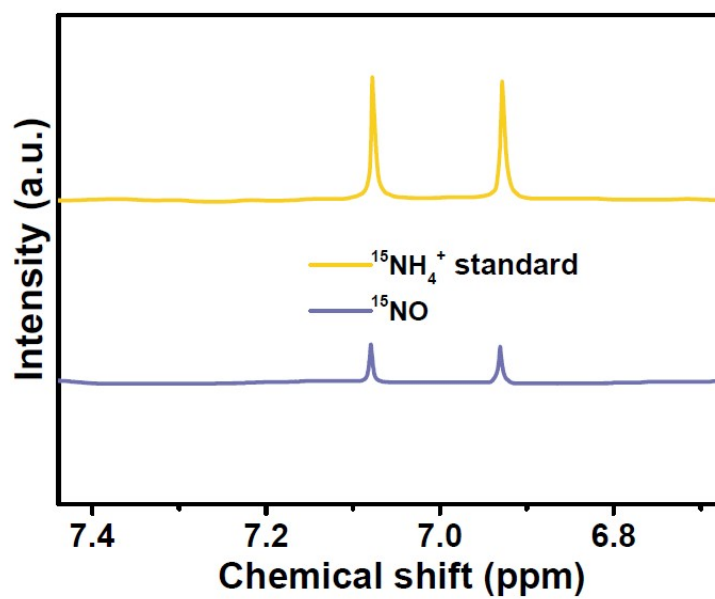
Fig. S16. ^1H NMR spectra of $^{15}NH_4^+$ standard sample and those fed by ^{15}NO and Ar after NORR electrolysis on $In_1/a\text{-}MoO_3$ at -0.6 V.
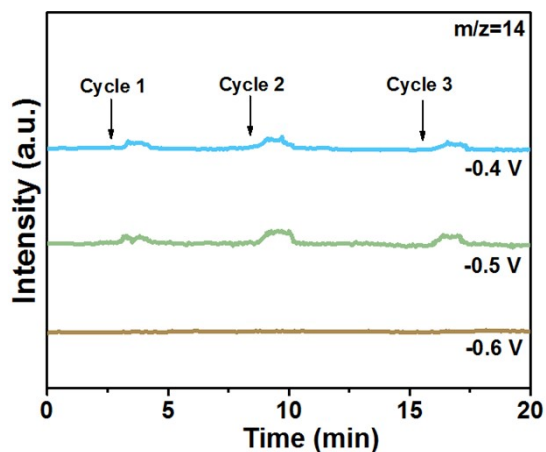
Fig. S17. Online DEMS spectra of In_1/a-MoO_3 during the electrolysis at -0.4 ~ -0.6 V.

It is seen that at -0.4 and -0.5 V, a small amount of *N intermediate is generated. These generated *N can be favorably coupled with *NO to generate N_2O by-product. However, the optimal NORR potential for our In_1/a-MoO_3 is -0.6 V, at which there is no *N intermediate generated, thus ruling out N_2O generation at -0.6 (Fig. 3c).

Initial snapshot **After simulation**

⌄ H_2O ●— NO   ○ H

Fig. S18. Initial and simulated states of the dynamic process of NO and H adsorption on In_1/a-MoO_3.
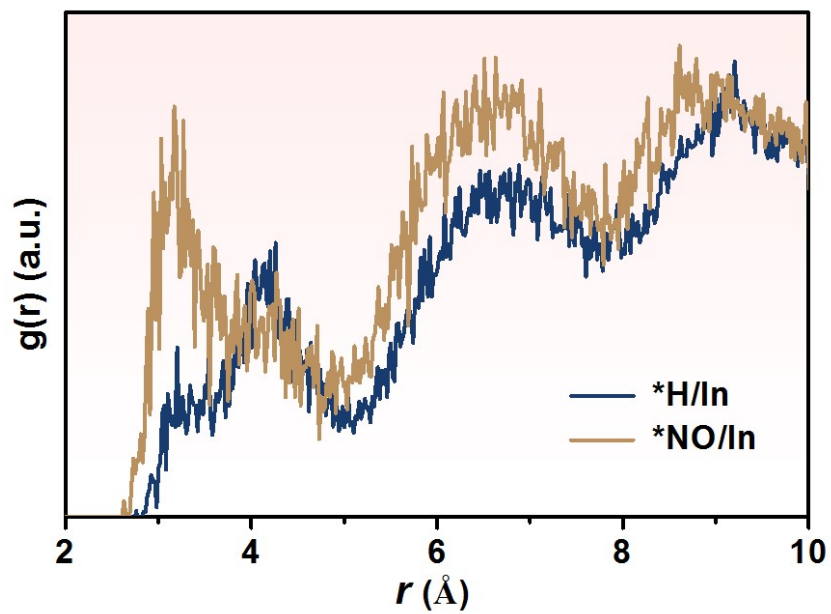
Fig. S19. RDF curves of the interactions between single-site In and *NO/*H.
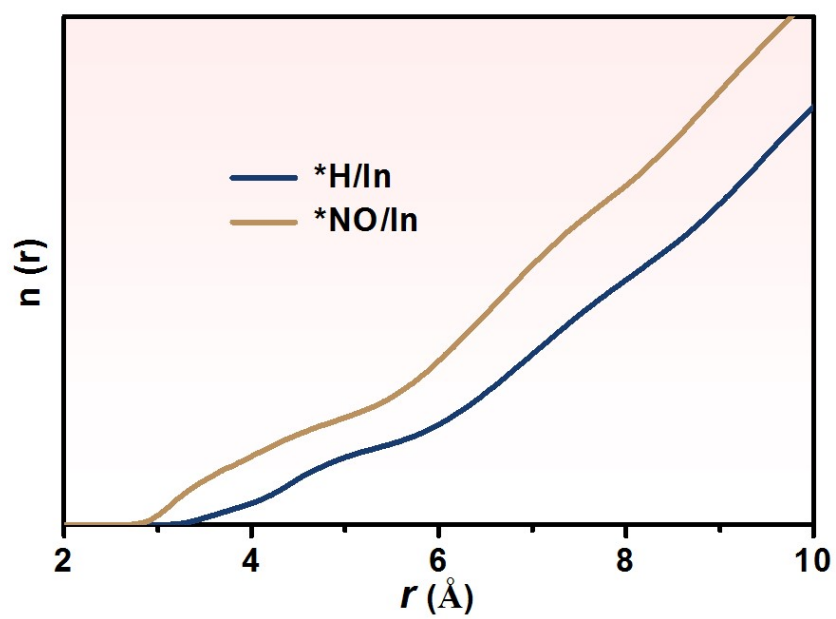
Fig. S20. Integrated RDF curves of the interactions between single-site In and *NO/*H.
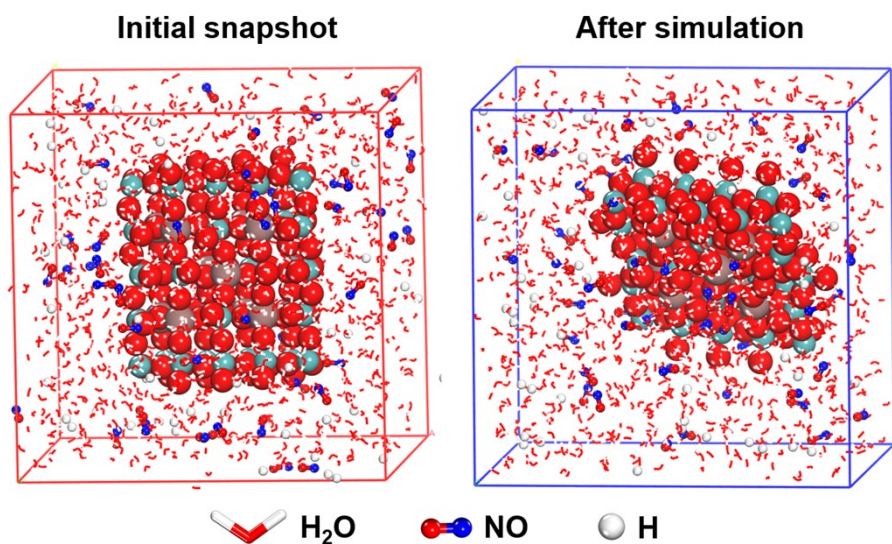
Table S1. Structural parameters extracted from the In K-edge EXAFS fitting.

Sample	Shell	CN	R (Å)	σ^2 (10^{-3}Å)	ΔE_0 (eV)	R factor
In$_1$/a-MoO$_3$	In-O	4.8	2.05	4.8	7.1	0.012

CN is the coordination number, R is interatomic distance, σ^2 is Debye-Waller factor, ΔE_0 is edge-energy shift, R factor is used to value the goodness of the fitting.

Table S2. Comparison of the optimum NH$_3$ yield and NH$_3$-Faradic efficiency (FE$_{NH3}$) for recently reported state-of-the-art NORR electrocatalysts at ambient conditions.

Catalyst	Electrolyte	NH$_3$ yield rate (μmol h^{-1} cm^{-2})	FE$_{NH3}$ (%)	Potential (V vs. RHE)	Ref.
Mo$_2$C	0.5 M Na$_2$SO$_4$	122.7	86.3	-0.4	[6]
Fe$_1$/MoS$_{2-x}$	0.5 M Na$_2$SO$_4$	288.2	82.5	-0.6	[7]
NiO/TM	0.1 M Na$_2$SO$_4$	125.3	90	-0.6	[8]
MoC/NCS	0.1 M HCl	79.4	89	-0.8	[9]
Cu$_2$O@CoMn$_2$O$_4$	0.1 M Na$_2$SO$_4$	94.18	75.05	-0.9	[10]
CoS$_{1-x}$	0.2 M Na$_2$SO$_4$	44.67	53.62	-0.4	[11]
Bi NDs	0.1 M Na$_2$SO$_4$	70.2	89.2	-0.5	[12]
Co$_1$/MoS$_2$	0.5M Na$_2$SO$_4$	217.6	87.7	-0.5	[13]
FeP/CC	0.2 M PBS	85.62	88.49	-0.2	[14]
CoP/TM	0.2 M Na$_2$SO$_4$	47.22	88.3	-0.2	[15]
a-B$_{2.6}$C@TiO$_2$/Ti	0.1 M Na$_2$SO$_4$	216.4	87.6	-0.9	[16]
Ni$_2$P/CP	0.1 M HCl	33.47	76.9	-0.2	[17]
In$_1$/a-MoO$_3$	**0.5 M Na$_2$SO$_4$**	**242.6**	**92.8**	**-0.6**	**This work**

Supplementary references

[1]. K. Chen, Y. Zhang, J. Xiang, X. Zhao, X. Li and K. Chu, *ACS Energy Lett.*, 2023, **8**, 1281-1288.

[2]. L. Zhang, J. Liang, Y. Wang, T. Mou, Y. Lin, L. Yue, T. Li, Q. Liu, Y. Luo, N. Li, B. Tang, Y. Liu, S. Gao, A. A. Alshehri, X. Guo, D. Ma and X. Sun, *Angew. Chem. Int. Edit.*, 2021, **60**, 25263-25268.

[3]. K. Chen, P. Shen, N. Zhang, D. Ma and K. Chu, *Inorg. Chem.*, 2023, **62**, 653-658.

[4]. P. Li, Z. Jin, Z. Fang and G. Yu, *Energy Environ. Sci.*, 2021, **14**, 3522-3531.

[5]. Y. Luo, K. Chen, P. Shen, X. Li, X. Li, Y. Li and K. Chu, *J. Colloid Interf. Sci.*, 2023, **629**, 950-957.

[6]. K. Chen, P. Shen, N. Zhang, D. Ma and K. Chu, *Inorg. Chem.*, 2023, DOI: 10.1021/acs.inorgchem.2c03714.

[7]. K. Chen, J. Wang, J. Kang, X. Lu, X. Zhao and K. Chu, *Appl. Catal. B*, 2023, **324**, 122241.

[8]. P. Liu, J. Liang, J. Wang, L. Zhang, J. Li, L. Yue, Y. Ren, T. Li, Y. Luo, N. Li, B. Tang, Q. Liu, A. M. Asiri, Q. Kong and X. Sun, *Chem. Commun.*, 2021, **57**, 13562-13565.

[9]. G. Meng, M. Jin, T. Wei, Q. Liu, S. Zhang, X. Peng, J. Luo and X. Liu, *Nano Res.*, 2022, **15**, 8890-8896.

[10]. C. Bai, S. Fan, X. Li, Z. Niu, J. Wang, Z. Liu and D. Zhang, *Adv. Funct. Mater.*, 2022, **32**, 2205569.

[11]. L. Zhang, Q. Zhou, J. Liang, L. Yue, T. Li, Y. Luo, Q. Liu, N. Li, B. Tang, F. Gong, X. Guo and X. Sun, *Inorg. Chem.*, 2022, **61**, 8096-8102.

[12]. Y. Lin, J. Liang, H. Li, L. Zhang, T. Mou, T. Li, L. Yue, Y. Ji, Q. Liu, Y. Luo, N. Li, B. Tang, Q. Wu, M. S. Hamdy, D. Ma and X. Sun, *Mater. Today Phys.*, 2022, **22**.

[13]. X. Li, K. Chen, X. Lu, D. Ma and K. Chu, *Chem. Eng. J.*, 2023, **454**, 140333.

[14]. J. Liang, Q. Zhou, T. Mou, H. Chen, L. Yue, Y. Luo, Q. Liu, M. S. Hamdy, A. A. Alshehri, F. Gong and X. Sun, *Nano Res.*, 2022, **15**, 4008-4013.

[15]. J. Liang, W.-F. Hu, B. Song, T. Mou, L. Zhang, Y. Luo, Q. Liu, A. A. Alshehri, M. S. Hamdy, L.-M. Yang and X. Sun, *Inorg. Chem. Front.*, 2022, **9**, 1366-1372.

[16]. J. Liang, P. Liu, Q. Li, T. Li, L. Yue, Y. Luo, Q. Liu, N. Li, B. Tang, A. A. Alshehri, I. Shakir, P. O. Agboola, C. Sun and X. Sun, *Angew. Chem. Int. Ed.*, 2022, **61**, e202202087.

[17]. T. Mou, J. Liang, Z. Ma, L. Zhang, Y. Lin, T. Li, Q. Liu, Y. Luo, Y. Liu, S. Gao, H. Zhao, A. M. Asiri, D. Ma and X. Sun, *J. Mater. Chem. A*, 2021, **9**, 24268-24275.